PERGAMON

International Journal of Solids and Structures 38 (2001) 759–775

INTERNATIONAL JOURNAL OF
SOLIDS and
STRUCTURES

www.elsevier.com/locate/ijsolstr

A study of stresses in powder compacted components during and after ejection

Pia Redanz *

Department of Solid Mechanics, Technical University of Denmark, Building 404, DK-2800 Lyngby, Denmark

Received 19 February 1999

Abstract

A finite strain finite element method is used to examine the residual stresses in a cup-shaped powder compact. Two rate-independent strain hardening porous material models are used: the combined material model (Fleck, N.A., Kuhn, L.T., McMeeking, R.M., 1992a. J. Mech. Phys. Solids 40 (5), 1139–1162) and a material model which includes the dependency of inter-particle cohesive strength (Fleck, N.A., 1995. J. Mech. Phys. Solids 43, 1409–1431). The residual stress state in the unloaded cup is highly dependent on the compaction process and less dependent on the ejection route. The maximum principal stress plotted during ejection shows that higher stresses are found during the ejection process than those found in the completely unloaded specimen. The degree of inter-particle cohesive strength has hardly any effect on the porosity distributions in the compacts but it has a strong influence on the stress state in the cups before unloading. However, after unloading, the stress states become quite similar in the two types of materials. © 2001 Elsevier Science Ltd. All rights reserved.

Keywords: Metal powder; Compaction; Residual stresses; Inter-particle cohesion

---

1. Introduction

Cold compaction of metal powders is widely used in industries. The ability to produce the required shape and dimensions of a component with very little or without subsequent machining is the main advantage compared to other production processes. The manufacture of a powder compacted component may roughly be divided into two steps. The first step is the compaction of the metal powder and the focus in the present work will be on cold die compaction where plastic deformation of the powder particles is the major deformation process. The second step is heat treatment or sintering of the compact in order to weld the powder particles together so that the component attains the desired strength. Hence, prior to sintering, the component is very fragile and fracture of the component may occur during ejection from the die.

In the beginning of the compaction process, the porous aggregate typically consists of distinct powder particles. Later in the process, the particles have deformed, and porosity now exists in the form of isolated voids. Based on the earlier work by Artz, Ashby and co-workers (Fischmeister et al., 1978; Artz, 1982; Helle

---

* Fax: +45-45-93-1475.
E-mail address: pia@fam.dtu.dk (P. Redanz).

PII: S0020-7683(00)00033-0

et al., 1985), Fleck et al. (1992a) proposed a micromechanically based particle model hereafter referred to as the FKM model. This model is appropriate at high porosities whereas the model of Gurson (1977) is pertinent for low porosities. In the transition range, a linear combination of the two models is used. This combined material model has been used earlier to study powder compaction of various simple geometries (Redanz, 1998) and the compaction of a cup (Redanz, 1999). In the latter, porosity dependence as well as applied load dependence on parameters such as matrix material behaviour, friction between mould and powder material, inter-particle cohesive strength, and different compaction schemes are studied. Neither Redanz (1998) nor Redanz (1999) considers the evolution of stresses during ejection or unloading. The material model has also been used to study ductile failure of a porous solid (Redanz et al., 1998; Redanz and Tvergaard, 1999).

In the present work, the compaction of the powder into a cup shape and the subsequent ejection of the cup have been modelled with a finite element programme in order to find the residual stress distribution in the green compact. Furthermore, the maximum principal stress during compaction and ejection has been determined to give insight into the risk of fracture during the process. Different compaction and ejection routes have been studied by varying the speed ratio of the punches. A straightforward method to model unloading of a compact numerically is to decrease the value of the nodal forces at the boundary to zero stepwise. In practice, one or more punches from one end of the compact are removed, and subsequently, the compact is ejected from the die by the punch at the other end. Both unloading and ejection are studied in the present paper.

Most material models in the literature are validated by comparing the porosity distribution from the model with experimental results. However, it has been shown (Redanz, 1999) with a modified version of the material model of Fleck (1995) that, before unloading, the porosity distributions are almost independent of the degree of inter-particle cohesion whereas the von Mises stress level is higher for a cohesionless compact than a compact with full inter-particle cohesion. The opposite tendency is noted for the effect of cohesion upon the hydrostatic pressure prior to unloading. Thus, justifying the use of a particular model by comparing density measurements with computational predictions may not be a critical test. More discriminating tests need to be devised which would allow the suitability of a given model to be determined. In the present work, the compacted cups are unloaded and the distribution of residual stresses is determined as a function of cohesion in order to determine whether the difference in stress states during compaction also exists after ejection from the die.

2. General equations

The analysis is based on a convected co-ordinate Lagrangian formulation of the field equations where g_{ij} and G_{ij} are the metric tensors in the reference and current frame, respectively, with determinants g and G. Here, the initial state is taken as reference. The Lagrangian strain tensor, $\eta_{ij} = 1/2(G_{ij} - g_{ij})$, in terms of the displacement components on the reference base vectors, u_i, is expressed by

$$\eta_{ij} = \tfrac{1}{2}(u_{i,j} + u_{j,i} + u^k_{,i} u_{k,j}) \tag{1}$$

in which $(\ )_{,i}$ denotes the covariant derivative.

Equilibrium is expressed in terms of the principle of virtual work which with body forces neglected takes the form

$$\int_V \tau^{ij}\, \delta\eta_{ij}\, \mathrm{d}V = \int_S T^i\, \delta u_i\, \mathrm{d}S. \tag{2}$$

Here, V and S are the volume and surface in the reference configuration and T^i are the components of the specified tractions per unit area in the reference configuration on the reference base vectors

$$T^i = (\tau^{ij} + \tau^{kj} u^i_{,k}) n_j \tag{3}$$

with n_j as the components of the surface normal in the reference state. The relation between the Kirchoff stress tensor, τ^{ij}, and the Cauchy or true stress tensor, σ^{ij}, is given by

$$\tau^{ij} = \sqrt{G/g}\,\sigma^{ij}, \tag{4}$$

where G/g denotes the volume change in the porous material.

The incremental constitutive relations for time-independent plasticity are of the form,

$$\dot{\tau}^{ij} = L^{ijkl} \dot{\eta}_{kl}, \tag{5}$$

where L^{ijkl} are the instantaneous moduli and $(\dot{\ })$ denotes differentiation with respect to a loading parameter.

The uniaxial true stress–logarithmic strain curve of the matrix material is expressed by the piecewise power law hardening expression

$$\epsilon = \begin{cases} \sigma/E, & \sigma \leqslant \sigma_{\mathrm{y}}, \\ \frac{\sigma_{\mathrm{y}}}{E}\left(\frac{\sigma}{\sigma_{\mathrm{y}}}\right)^n, & \sigma > \sigma_{\mathrm{y}}, \end{cases} \tag{6}$$

where ϵ is the logarithmic strain, σ is the true stress, σ_{y} is the uniaxial yield stress and n is the strain hardening exponent. The material approaches an elastic-perfectly plastic material for very large n.

Contact and friction between the powder and the tool play an important role in the powder compaction process. The contact between the powder and the die (or the punch) is modelled by a penalty method using elastic springs of high stiffness, see e.g. Tvergaard (1990). When the material is in contact with the die or punches, the state of friction may be either sticking or sliding. Sticking contact is modelled the same way as the contact constraint, whereas frictional sliding is modelled by the following expression

$$T_{\mathrm{t}} = \begin{cases} -\mathrm{sgn}(\dot{u}_{\mathrm{t}})\mu T_{\mathrm{n}} & |\mu T_{\mathrm{n}}| < \sigma_{\mathrm{y}}/\sqrt{3} \\ \mathrm{sgn}(\dot{u}_{\mathrm{t}})\sigma_{\mathrm{y}}/\sqrt{3} & |\mu T_{\mathrm{n}}| > \sigma_{\mathrm{y}}/\sqrt{3} \end{cases} \quad \text{for} \quad \dot{u}_{\mathrm{t}} \neq 0,\ T_{\mathrm{n}} < 0. \tag{7}$$

Here, T_{n} and T_{t} are the normal and tangential tractions, respectively, $\dot{u}_{\mathrm{t}}$ is the incremental displacement difference in the tangential direction and μ is the friction coefficient. At lower normal pressures, the Coulomb friction model is used. However, at normal pressures where μT_{n} exceeds the shear yield stress of the material, the friction stress is kept constant. The chosen upper limit for the friction stress, $\sigma_{\mathrm{y}}/\sqrt{3}$, is an approximation and neglects any dependency upon porosity and strain hardening of the material.

3. Porous material models

3.1. Combined FKM and Gurson material model

The microstructure of the porous aggregate changes during compaction. In the beginning of the process, the aggregate consists of loose powder particles whereas later in the process the particles have deformed and a void-like morphology appears.

At high porosities, $f > f_1$, a particle-based material model, the FKM model of Fleck et al. (1992a), is used. It assumes that spherical particles in point contact form the porous material and has the yield function

$$\Phi_{\mathrm{FKM}} = \left(\frac{5}{18}\frac{\sigma_{\mathrm{e}}}{p_{\mathrm{y}}} + \frac{2}{3}\right)^2 + \left(\frac{\sqrt{5}}{3}\frac{\frac{1}{3}\sigma^k_k}{p_{\mathrm{y}}}\right)^2 - 1 = 0 \tag{8}$$

with the macroscopic effective von Mises stress given by $\sigma_e = (3s_{ij}s^{ij}/2)^{1/2}$ in which $s^{ij} = \sigma^{ij} - G^{ij}\sigma^k_k/3$ is the stress deviator, σ_M is the current yield stress of the matrix material and p_y denotes the yield strength of the porous material under hydrostatic loading:

$$p_y = 2.97(1-f)^2 \frac{\hat{f} - f}{\hat{f}} \sigma_M. \tag{9}$$

The highest possible porosity in this model is $f = \hat{f} = 0.36$, corresponding to the dense random packing of equi-sized spheres (Helle et al., 1985). At lower porosities, the contacts start to interact and the particles become less spherical in shape. Thus, the FKM model is valid at higher porosities only.

The second material model in the combined model is an elastic-strain hardening plastic version of the model of Gurson (1977). This model is used upon porosities lower than f_2, $f < f_2$, and has the following form:

$$\Phi_{\text{Gurson}} = \frac{\sigma_e^2}{\sigma_M^2} + 2q_1 f \cosh\left\{\frac{q_2}{2}\frac{\sigma^k_k}{\sigma_M}\right\} - \left(1 + (q_1 f)^2\right) = 0. \tag{10}$$

Here, q_1 and q_2 are adjustable parameters suggested by Tvergaard (1981, 1982), and following his recommendation, are set to 1.5 and 1.0, respectively, in the present study. The Gurson model is based on the assumption that porosity exists in the form of spherical voids and the model reduces to J_2 flow theory when $f = 0$.

In the transition range, $f_1 > f > f_2$, a linear combination of the FKM and Gurson models is used with the yield criterion

$$\Phi_{\text{comb}} = W_{\text{FKM}}\Phi_{\text{FKM}} + W_{\text{Gurson}}\Phi_{\text{Gurson}} = 0, \tag{11}$$

where the weight functions are given by $W_{\text{FKM}} = (f - f_2)/(f_1 - f_2)$ and $W_{\text{Gurson}} = (f_1 - f)/(f_1 - f_2)$. The parameters defining the transition range are chosen as (Fleck et al., 1992a), $f_1 = 0.25$ and $f_2 = 0.1$.

3.2. Material model with variable inter-particle cohesion

Many compaction models (e.g. Gurson, 1977; Shima and Oyane, 1976; Fleck et al., 1992a) assume that the porous material has equal tensile and compressive strengths, partly because these models have been developed for the study of ductile fracture. Other models assume a vanishing or a small cohesive strength between the particles, e.g. soil mechanics models such as the Cam–Clay model (Schofield and Wroth, 1968) or the Drucker–Prager model (1952). In the compaction of metal powders, the inter-particle cohesive strength lies between these ideal limits. Fleck (1995) proposed a material model with a variable degree of inter-particle cohesion and introduced the cohesion factor, η, for which fully sticking contacts are obtained when $\eta = 1$ and zero cohesive strength is present at $\eta = 0$. In order to obtain a yield surface in closer agreement with experimental compaction studies of copper powder (Akisanya et al., 1997), a modified version of material model of Fleck (1995) with variable inter-particle cohesion was suggested (Redanz, 1999). This modified approximate yield surface has the following form:

$$\Phi = \left(\frac{5}{18}\frac{\sigma_e}{p_y} + \frac{2}{3}\right)^2 + \left(\frac{\sqrt{5}}{3}\frac{\frac{1}{3}\sigma^k_k}{p_y}\right)^2 \frac{5}{9}(1-\eta)\left(1 + \frac{\frac{1}{3}\sigma^k_k}{p_y} - \frac{1}{3}\frac{\sigma_e}{p_y}\right) - 1 = 0. \tag{12}$$

At fully sticking contacts, $\eta = 1$, the modified yield surface reduces to the FKM yield surface. The modified model (12) is valid at higher porosities only since the combined form (11) with the Gurson model is no longer physically consistent at low porosities.

3.3. Basic porous material equations

The direction of the plastic strain is assumed to be normal to the yield surface

$$\dot{\eta}_{ij}^{\mathrm{P}} = \Lambda \frac{\partial \Phi}{\partial \sigma^{ij}}, \tag{13}$$

where Λ is the plastic multiplier and $\partial \Phi / \partial \sigma^{ij}$ gives the direction of the plastic flow. The initiation of plastic yielding occurs when $\Phi = 0$ and $\dot{\Phi} > 0$. During plastic yielding, the consistency condition must be fulfilled

$$\dot{\Phi} = \frac{\partial \Phi}{\partial \sigma_{\mathrm{e}}} \dot{\sigma}_{\mathrm{e}} + \frac{\partial \Phi}{\partial \sigma_k^k} \dot{\sigma}_k^k + \frac{\partial \Phi}{\partial f} \dot{f} + \frac{\partial \Phi}{\partial \sigma_{\mathrm{M}}} \dot{\sigma}_{\mathrm{M}} = 0 \tag{14}$$

in which the evolution equation for $\dot{\sigma}_{\mathrm{M}}$ is found from equivalent plastic work to be of the form

$$\dot{\sigma}_{\mathrm{M}} = \frac{E E_{\mathrm{t}}}{E - E_{\mathrm{t}}} \frac{\sigma^{ij} \dot{\eta}_{ij}^{\mathrm{P}}}{F(f) \sigma_{\mathrm{M}}}. \tag{15}$$

Here, E_{t} is the slope of the uniaxial true stress–logarithmic strain curve for the matrix material, and $F(f)$ represents the volume fraction of deforming material, which depends on the yield criterion used. The contribution from the elastic part of the strain to the total change in volume is neglected compared to the plastic contribution. Hence, the change in porosity may be written

$$\dot{f} = (1 - f) G^{ij} \dot{\eta}_{ij}^{\mathrm{P}}. \tag{16}$$

Using Eqs. (13)–(16), the plastic multiplier, Λ, is found, and Eq. (13) can be written in the form

$$\dot{\eta}_{ij}^{\mathrm{P}} = \frac{1}{H} \frac{\partial \Phi}{\partial \sigma^{ij}} \frac{\partial \Phi}{\partial \sigma^{kl}} \overset{\nabla}{\sigma}{}^{kl} \tag{17}$$

with $\overset{\nabla}{\sigma}{}^{kl}$ as the Jaumann rate of the Cauchy stress tensor and

$$H = -\left(\frac{\partial \Phi}{\partial f} (1 - f) G^{ij} + \frac{\partial \Phi}{\partial \sigma_{\mathrm{M}}} \frac{E E_{\mathrm{t}}}{E - E_{\mathrm{t}}} \frac{\sigma^{ij}}{F(f) \sigma_{\mathrm{M}}} \right) \frac{\partial \Phi}{\partial \sigma^{ij}}. \tag{18}$$

The total strain is taken to be the sum of the elastic and plastic parts. Thus, from the elastic constitutive relations (see e.g. the hypo-elastic relations in Hutchinson (1973)) and Eq. (17), the instantaneous moduli from Eq. (5) are determined.

The dependence of the elastic parameters on porosity can normally be neglected in the modelling of powder compaction because the plastic strains overwhelm the elastic strains. However, when ejection of the specimen from the die is studied, elastic unloading of the material occurs, and thus, the elastic material properties are important. In the present work, Poisson's ratio is assumed to equal that of the matrix material, $\nu = \nu_{\mathrm{M}}$, and Young's modulus, E, is assumed to depend linearly on porosity,

$$E = E_{\mathrm{i}} + (E_{\mathrm{M}} - E_{\mathrm{i}}) \frac{\hat{f} - f}{\hat{f}}, \tag{19}$$

where E_{M} is Young's modulus of the matrix material and E_{i} is Young's modulus of the porous aggregate at $f = \hat{f}$; the latter is set here to $E_{\mathrm{i}} = 0.0014 E_{\mathrm{M}}$. This assumption differs slightly from the dependence used by Fleck et al. (1992b) in the sense that the stiffness of the porous aggregate is not equal to zero at dense random packing, $f = \hat{f}$, but is slightly higher. By choosing a finite initial modulus, E_{i}, the computation time is decreased significantly and numerical difficulties are avoided. As a consequence, the early elastic stage of the compaction (at porosities close to $f = \hat{f}$) is not modelled, but as the plastic deformation is dominant in the present work, this has nearly no influence on the results; see also Mesarovic (1999).

4. Numerical method

In the current state, σ^{ij}, η_{ij}, etc. satisfy the equilibrium which is expressed in terms of the principle of virtual work (2). An incrementally linear, forward extrapolation scheme is used to determine the incremental values, $\dot{\sigma}^{ij}$, $\dot{\eta}_{ij}$, etc. Thus, the principle of virtual work is extended about the current state to the incremental form

$$\int_V \left\{ \dot{\tau}^{ij}\,\delta\eta_{ij} + \tau^{ij}\dot{u}^k_{,i}\delta u_{k,j} \right\} \mathrm{d}V = \int_S \dot{T}^i\,\delta u_i\,\mathrm{d}S - \left[\int_V \tau^{ij}\,\delta\eta_{ij}\,\mathrm{d}V - \int_S T^i\,\delta u_i\,\mathrm{d}S \right] \tag{20}$$

with body forces neglected. The term in square brackets corresponds to the principle of virtual work in total form (2) and thus should equal zero. It is included here in order to prevent the numerical solution from drifting away from equilibrium due to an accumulation of incremental errors.

The axisymmetric compaction tool and powder material are modelled numerically as shown in Fig. 1(a). The three punches, P_1, P_2, and P_3, may be moved independently at different speeds. The powder is filled into the mould while it is turned upside down, so that, due to gravity, the powder initially forms a cup shape. Overviews of the die movement sequences in the various compaction and ejection routes are listed in Tables 1 and 2, respectively.

One of the initial finite element meshes is shown in Fig. 1(b). Each mesh used in the present study consists of 396 isoparametric, eight-noded elements with a total of 1279 nodes. Each element contains four integration points. For all of the results presented, the powder material is characterized by the material parameters, $\sigma_y/E = 0.003$, $n = 10$, $\nu = 1/3$, and the initial porosity is $f = 0.35$. The value of the friction coefficient, μ, from Eq. (7) has been found experimentally for the compaction of a simple cylinder by Kim et al. (1996) to be 0.17, and this value is used here.

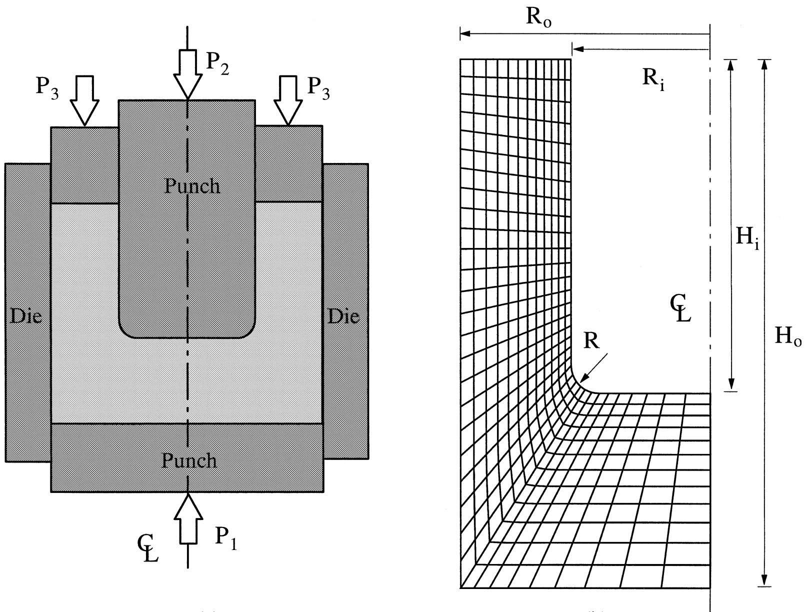

(a) (b)

Fig. 1. (a) The axisymmetric compaction model consists of a die and three individual punches P_1, P_2 and P_3, (b) the initial finite element mesh used for *compaction I* consists of 396 isoparametric eight noded elements with a total of 1279 nodes.

Table 1
The various sequences of die movement in *Compactions I–III* on the left side of the table[a] and the total displacements of the punches on the right side of the table

	Displacement of punches			Total displacements	
	P_1	P_2	P_3	Figs. 2–7	Figs. 8–11
Compaction I	u_{I}	0	u_{I}	$u_{\mathrm{I}}/R = 2.00$	–
Compaction II	u_{II}	0	$\frac{1}{2}u_{\mathrm{II}}$	$u_{\mathrm{II}}/R = 2.51$	–
Compaction III	u_{III}	0	$2u_{\mathrm{III}}$	$u_{\mathrm{III}}/R = 1.42$	$u_{\mathrm{III}}/R = 0.96$

[a] The die wall is held fixed at all times.

Table 2
An overview of the various sequences of die movement in *Ejections I and II*[a]

	Step 1	Step 2	Step 3
Ejection I	P_1 is taken off	P_2 and P_3 eject the cup	P_2 is taken off
Ejection II	P_3 is taken off	P_1 ejects the cup	P_2 is taken off

[a] The die wall is held fixed at all times.

5. Results

5.1. The first stage of the process: compaction

The porosity distributions in the powder compacts due to three different compaction routes are shown in Fig. 2. The outlines of the initial cup geometries are shown with dotted lines, whereas the deformed cup shapes after unloading are marked with solid lines. In Fig. 2(a), punches P_1 and P_3, from Fig. 1(a), are moved with the same speed, while the inner punch, P_2, is held still. This compaction route is referred to as ‘compaction I’ in the following. In ‘compaction II’, the punch on the wall of the cup, P_3, is moved with half the speed of the punch at the bottom of the cup, P_1, while P_2 is held fixed; the resulting porosity distribution is shown in Fig. 2(b). In ‘compaction III’, the punch P_3 is moved with twice the speed of P_1, while P_2 is fixed; see Fig. 2(c) for the resulting porosity distribution. The initial volume of each cup is the same, whereas the initial geometry differs in each case in order to obtain the same geometry and volume of the specimens after compaction. For the initial geometries of the cups, see Table 3. The cups have been compacted to a volume change $\Delta V/V_0 = 0.22$, where ΔV is the difference between initial and current volume, and V_0 is the initial volume of the cup, see also Table 1.

It should be noted that the porosity distributions change only slightly during unloading and do not therefore depend on how the cups are ejected from the die. Hence, the elastic spring-back effect is negligible in the present study.

In all the three cases, regions with highly compacted material develop at the corners between punches and die wall due to friction. The effect of double-action pressing is also seen in each of the porosity distributions. In Fig. 2(a), a region with less compacted material appears in the cup wall midway between the upper and lower punches. A similar region of reduced compaction exists higher up the cup wall in Fig. 2(b) and lower down the cup wall in Fig. 2(c): the precise location depends on the velocity ratio between P_1 and P_3. Due to the geometry of the cup as well as the double action compaction scheme, a region with packed material at the bottom in the inside of the cup, see point A in Fig. 2(a), and a less compacted region in the cup wall on the vertical face adjacent to the corner, see point B, are formed. When P_1 is moved faster than P_3, *compaction II* in Fig. 2(b), this effect becomes more dominant, whereas it is almost avoided in Fig. 2(c) where P_1 is moved with half the speed of P_3, *compaction III*. In general, the porosity gradients in case of *compaction II* are higher compared to *compaction I* whereas *compaction III* results in the most uniform

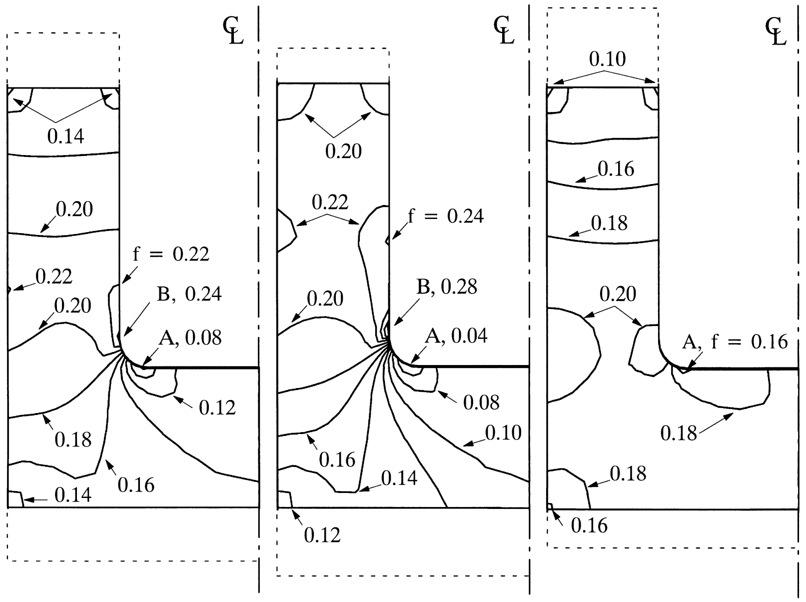

Compaction I
(a)

Compaction II
(b)

Compaction III
(c)

Fig. 2. Curves of constant porosity, f, as results of three different compaction routes at $\Delta V/V_0 = 0.22$: (a) *Compaction I*, P_1 and P_3 are moved with the same speed while P_2 is fixed, (b) *Compaction II*, P_3 is moved with half the speed of P_1 while P_2 is fixed and (c) *Compaction III*, P_3 is moved with twice the speed of P_1 while P_2 is fixed.

Table 3
The various initial cup geometries used for *Compactions I to III*[a]

	Initial cup geometries			
	R_i/R	R_o/R	H_i/R	H_o/R
Compaction I	5	9	12	19
Compaction II	5	9	11.26	18.77
Compaction III	5	9	12.84	19.26

[a] The parameters are defined in Fig. 1(b).

porosity distribution of the three. As shown in Redanz (1999), the average porosity decreases during compaction, whereas the way this porosity is distributed remains approximately the same until fully dense regions are formed. Under continued loading, these fully dense regions spread until full densification is obtained. However, full densification is rarely obtained in practice.

5.2. The second stage of the process: ejection

In the practical powder compaction process, the powder is mixed with a binder to bond the particles together in order to obtain some degree of inter-particle cohesion. This minimizes the risk of fracture of the compact during the subsequent ejection. During the compaction process, the areas of particle contacts weld together and form metallurgical bonds (Dowson, 1990). However, these bonds are fairly weak at process temperatures lower than 0.3 times the absolute melting temperature of the powder material (cold compaction). Hence, in the present study, brittle fracture during ejection is likely to occur depending on the maximum principal stress, $\max(\sigma_i)$.

The simplest way to develop residual stresses in a numerical simulation of compaction is to reduce the nodal forces at the boundary stepwise to zero; in the following, this is referred to as *boundary unloading*. The maximum principal stress normalized by the initial yield stress of the matrix material in tension, $\max(\sigma_i/\sigma_y)$, is shown for the three different compaction routes and subsequent *boundary unloading* in Fig. 3. Unless otherwise stated, the point at which the maximum principal stress occurs is located at the inner rounded corner of the cup. The solid line, representing *compaction I*, shows that the maximum principal stress oscillates about zero during compaction. During *boundary unloading*, the normalized stress increases from about zero to approximately 0.4. At each point where the curves change abruptly, either the location at which the maximum stress has occurred changes or the direction of the maximum principal stress changes. When *compaction II* is used, the maximum principal stress is tensile throughout the compaction process and it increases to $\max(\sigma_i/\sigma_y) = 0.95$ during *boundary unloading* which may result in the formation of a crack at the rounded, inner corner of the cup. During *compaction III*, the stress is compressive throughout the process and reaches $0.15\sigma_y$ after *boundary unloading*. As concluded from the discussion of Fig. 2, *compaction III* is the optimal compaction route of the three.

In practice, unloading the specimen after die compaction as described above is not possible. The ejection and handling of the fragile green specimen is often the weakest link in the process of a powder metallurgy component. The maximum principal stress for the three compaction routes and the subsequent evolution of the stresses during ejection are shown in Fig. 4. The ejection route, referred to as *ejection I*, goes as follows: first, P_1 is removed, followed by ejection of the specimen from the die by P_2 and P_3. Finally, the inner punch, P_2, is taken out of the cup.

When P_1 is removed, the maximum principal stress remains approximately zero in the case of *compaction I* until right before the punch is completely removed. Then, the stress increases abruptly to

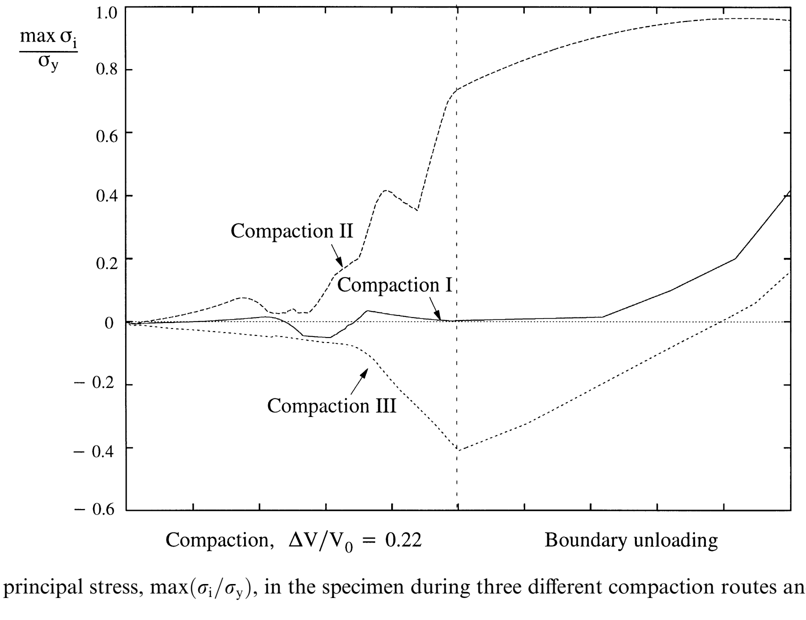

Fig. 3. The maximum principal stress, $\max(\sigma_i/\sigma_y)$, in the specimen during three different compaction routes and subsequent *boundary unloading*.

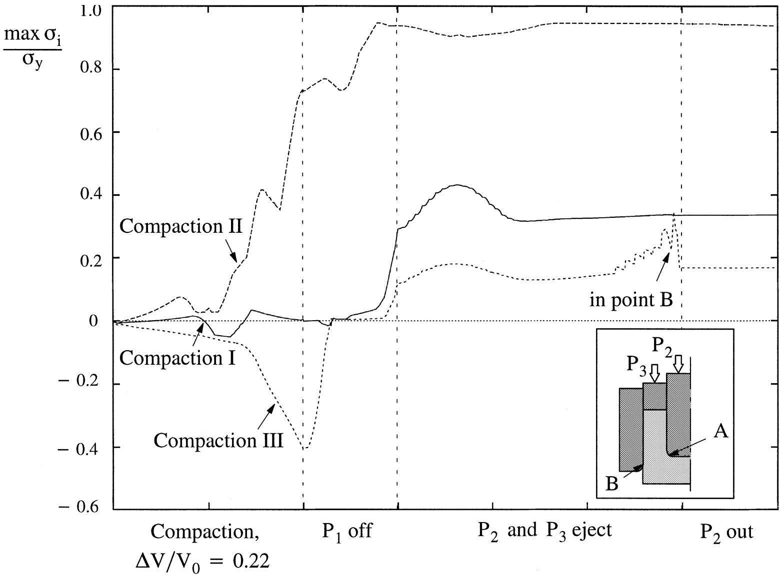

Fig. 4. The maximum principal stress, $\max(\sigma_i/\sigma_y)$, in the specimen during three different compaction routes and subsequent unloading, *ejection I*.

$\max(\sigma_i/\sigma_y) = 0.35$. During the ejection of the specimen from punches P_2 and P_3, the stress increases to a peak value, $\max(\sigma_i/\sigma_y) = 0.43$, and decreases afterwards to 0.35. The peak value is reached when the bottom of the cup is about halfway out of the die. The pressure between the specimen and the punch, P_2, is reduced to zero during the ejection, thus, the stress state does not change upon final removal of P_2. The small oscillations of the curve are due to the discreteness of the finite element mesh; each oscillation corresponds to a node losing contact with the die wall. This contact transition has been eased by rounding-off the edge of the die wall with a radius equal to $1.30H_o$. A smaller radius results in oscillations of higher amplitude and vice versa.

When P_l is taken-off after *compaction II*, the maximum principal stress increases; thereafter, the maximum principal stress remains fairly constant at the same level as was found for *boundary unloading*, $\max(\sigma_i/\sigma_y) = 0.95$, during ejection from the die.

The high compressive stress after *compaction III* decreases until it reaches zero when P_l is removed. After having plateaued at zero, the stress increases in tension to $\max(\sigma_i/\sigma_y) = 0.15$ just before P_l is completely removed, as was also seen for *compaction I*. A minor stress peak is reached in the beginning of the ejection and a larger stress peak is attained at the end of the ejection. Again, the oscillations are due to the discreteness of the mesh. As mentioned above, the maximum principal stress is mostly located at the inner, rounded corner of the cup, see label A in the insert to Fig. 4. However, the large stress peak at the end of ejection is located in the cup wall in the region following the edge of the die wall as the specimen is ejected, see label B. This stress increase might easily result in a chipped corner at the top of the cup wall. The stress concentration by the edge of the die wall is also present in the two other cases, but the trajectories in Fig. 4 refer to the stress state at the inner corner since it is largest. Removal of the inner punch, P_2, hardly changes the stress state. In practice, it is sometimes necessary to eject the specimen from the die with the relative positions of all punches held fixed; subsequently, the punches are taken-off. This reduces the tensile stresses during ejection and damage or fracture of the component may be avoided. Furthermore, the edge of the die wall is rounded-off in order to minimize stress concentrations like that in point B, (Fig. 4). This is also done in the present numerical study.

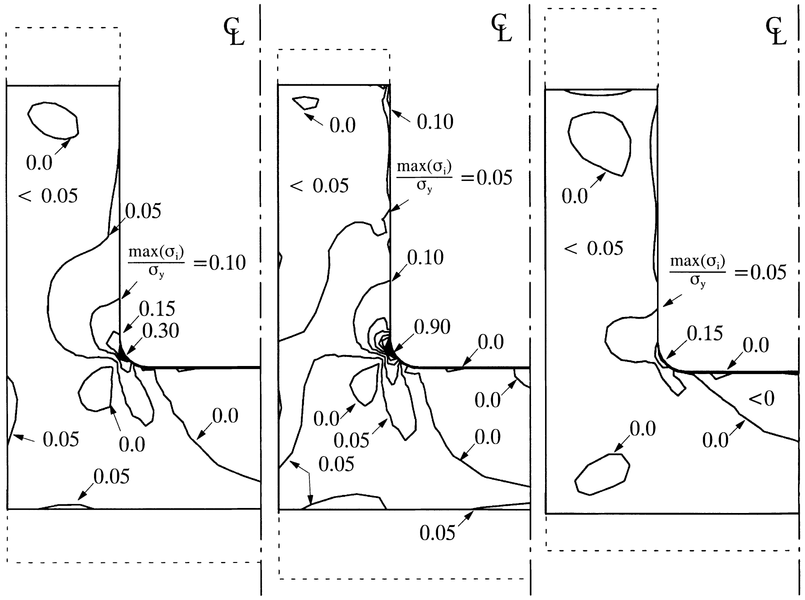

Compaction I
(a)

Compaction II
(b)

Compaction III
(c)

Fig. 5. Curves of constant maximum principal stress, $\max(\sigma_i)/\sigma_y$, at $\Delta V/V_0 = 0.22$, after three different compaction routes and subsequent unloading, *ejection I*.

The stress states in the three specimens after *ejection I* are shown in Fig. 5. Curves of constant maximum principal stress normalized by the yield stress of the matrix material, $\max(\sigma_i/\sigma_y)$, are shown for *compaction I*, *compaction II*, and *compaction III* in Fig. 5(a)–(c), respectively. For the case of *compaction I*, the maximum principal stress attains a maximum value, $\max(\sigma_i/\sigma_y) = 0.30$, at the inner, rounded corner and is close to zero elsewhere. The stress distribution as a result of *compaction II* is similar qualitatively but is more extreme in value. Here, the principal stress attains values up to $0.9\sigma_y$, with a maximum value at the inner, rounded corner. Also, a stress concentration in the inner, upper edge of the cup wall is present. *Compaction III* results in a fairly uniform maximum principal stress distribution and close to zero in magnitude.

In Fig. 6, the evolution of the maximum principal stresses during the first compaction route, *compaction I*, and different subsequent types of unloading are shown. The *boundary unloading* and *ejection I* have already been described above; *Ejection II* refers to the following: P_3 is taken-off, P_1 ejects the cup from the die and then P_2 is taken out. Removal of P_3 in the first stage of *ejection II* results in a larger maximum stress than removal of P_1 in the first stage of *ejection I*. While P_1 ejects the cup from the die in *ejection II*, this high stress remains fairly constant. Unlike *ejection I*, the removal of the inner punch, P_2, in *ejection II* leads to a stress decrease. The *boundary unloading* results in a higher final maximum principal stress compared to both ejection routes; however, this stress value is lower than the peak stress observed during *ejection I*.

The influence of the different ejection routes on the residual stress distributions in the powder compacts obtained with *compaction I* is illustrated in Fig. 7. It is seen that the distributions for *ejection I*, Fig. 5(a), and *boundary unloading*, Fig. 7(a), are almost identical, whereas the stress state in the cup after *ejection II*, Fig. 7(b), differs from the two others. When P_1 ejects the compact in *ejection II* the separation of the inner punch, P_2, and the ejecting punch, P_1, is fixed. Thus, the cup is subjected to an applied stress in the axial

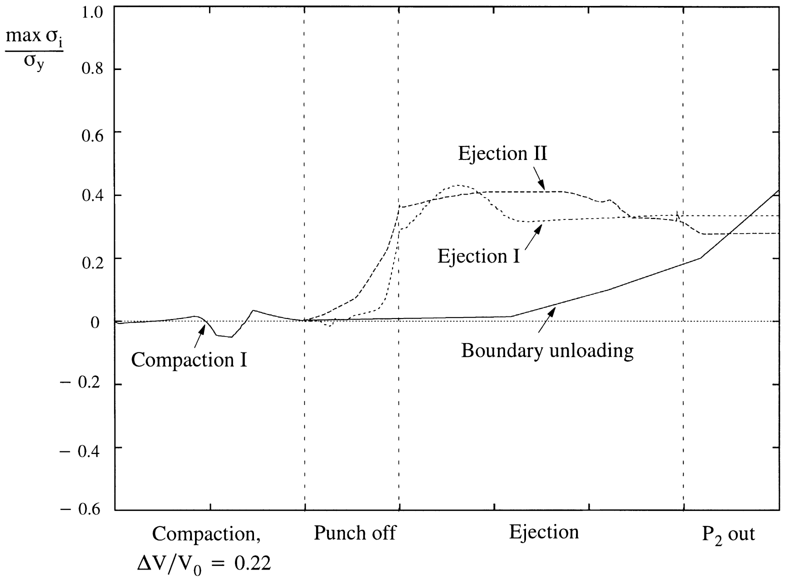

Fig. 6. The maximum principal stress, $\max(\sigma_i/\sigma_y)$, in the specimen during compaction, *compaction I*, and three different unloading routes.

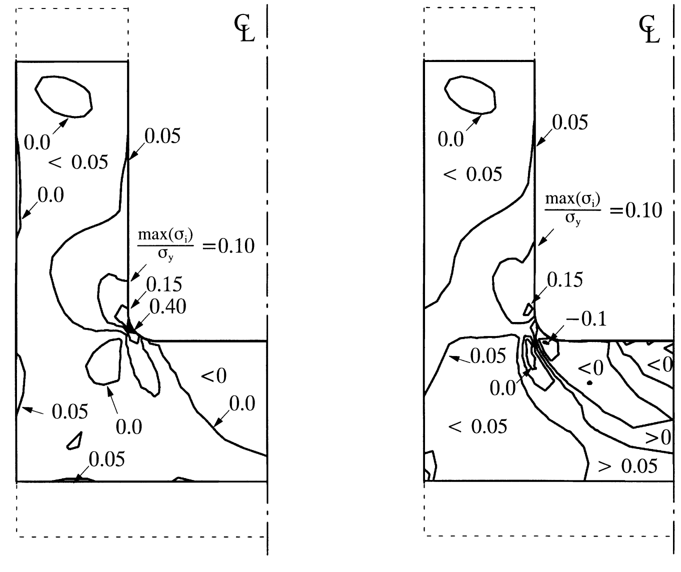

Compaction I + Boundary unloading

(a)

Compaction I + Ejection II

(b)

Fig. 7. Curves of constant maximum principal stress, $\max(\sigma_i)/\sigma_y$, at $\Delta V/V_0 = 0.22$, after *compaction I* and two different unloading paths, *boundary unloading* and *ejection II*.

direction during ejection which is not the case in *ejection I*. For *ejection II*, this results in higher maximum principal stresses in the bottom of the cup and a region with entirely compressive stresses just below the inner rounded corner of the cup. Furthermore, a stress concentration develops in the corner between the die wall and the ejecting, lower punch, P_1. For all three ejection routes, the residual maximum principal stresses in the cup walls are mainly tensile but with an enclosed region with material in compression. Ejecting the specimen from one side or the other affects the residual stress distribution in the present case. However, this is mainly due to the externally applied axial pressure from the inner punch, P_2, during *ejection II.* In summary, the simple boundary unloading method provides a useful guide in predicting the residual stress distribution but it does not capture the evolution of the maximum principal stress during ejection which may exceed the final value in the specimen when completely ejected from the tool.

5.3. The effect of inter-particle cohesive strength

The effect of inter-particle cohesive strength is now studied with the modified material model (Fleck, 1995; Redanz, 1999). This model is not combined with the Gurson model, thus, it is valid at high porosities only. The optimal compaction route from the above study, *compaction III*, has been used to compact two cups of powder materials with different inter-particle cohesive strengths to a volume change, $\Delta V/V_0 = 0.14$. After compaction, the porosity distributions are very similar to the one shown in Fig. 2(c), whereas the average porosity is higher due to the lower degree of compaction.

The von Mises stress distributions in the cups before unloading are shown in Fig. 8. A material with fully sticking contacts between the powder particles, $\eta = 1$, is shown in Fig. 8(a), and a material with a low cohesive strength, $\eta = 0.2$, is shown in Fig. 8(b). It is seen that the relative distributions are somewhat similar to each other: stress concentrations in the corners between the punches and die wall and at the rounded edge at the inside of the cup. However, the stress level in the material with fully sticking contacts is much higher compared to the low cohesive strength powder material. The opposite is the case for the hydrostatic pressure in the cup before ejection. A similar result was seen in Redanz (1999). As both the von

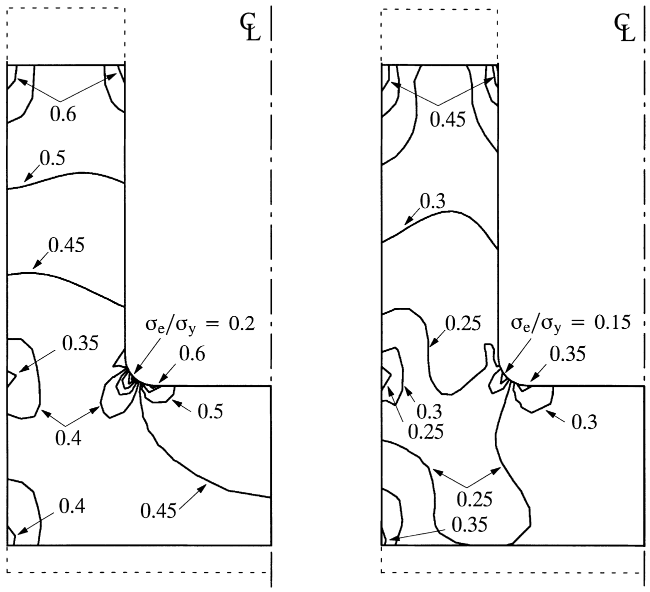

(a) (b)

Fig. 8. Curves of constant von Mises stress, σ_e/σ_y, at $\Delta V/V_0 = 0.14$ after *compaction III* before unloading: (a) fully sticking contacts between the powder particles, $\eta = 1$ and (b) low inter-particle cohesive strength, $\eta = 0.2$.

Mises stress and the hydrostatic pressure lead to plastic yielding in a porous solid, it is not surprising that similar porosity distributions can develop in compacts of materials with different inter-particle cohesive strengths even though the stress states are different.

The maximum principal stress in the cups during the process is shown in Fig. 9. It is seen that the stresses in both cases are compressive throughout the compaction. The maximum principal stress in the material with low cohesive strength is significantly lower than the stress in the fully sticking contacts powder material. After *boundary unloading*, it is seen from Fig. 9 that the final maximum principal stress value in the low cohesive material specimen is tensile and higher than the final value in the cup of fully sticking contacts powder material. A low tensile stress in a material with little cohesive strength may rapidly lead to fracture. The stress in the fully sticking material also goes slightly into the tensile region, but as the material has a high cohesive strength in tension this is of less concern. Throughout both compaction and unloading of the two types of material, the maximum principal stress was located at the inner rounded corner of the cup.

The effective stress, σ_e/σ_y, in the cups after *boundary unloading* are shown in Fig. 10. Both the level and the distribution of the von Mises stress are strikingly similar in the two types of material unlike the stress states before unloading, compare with Fig. 8. Upon unloading, a stress concentration is present in the outer side of the cup wall midway between the upper and lower punches in the region with less compacted material. A stress concentration is also present at the inner rounded corner of both cups. For the material with full cohesive strength between the particles, $\eta = 1$, (Fig. 10(a)), the maximum von Mises stress is located slightly lower than for the case with $\eta = 0.2$, (Fig. 10(b)).

Finally, the maximum principal stress contours in the unloaded cups are shown in Fig. 11(a) and (b) for the material with fully sticking contacts, $\eta = 1$, and the material with low inter-particle cohesive strength, $\eta = 0.2$, respectively. In both cases, the maximum principal stresses in the cups are close to zero except in the region at the inner rounded corner.

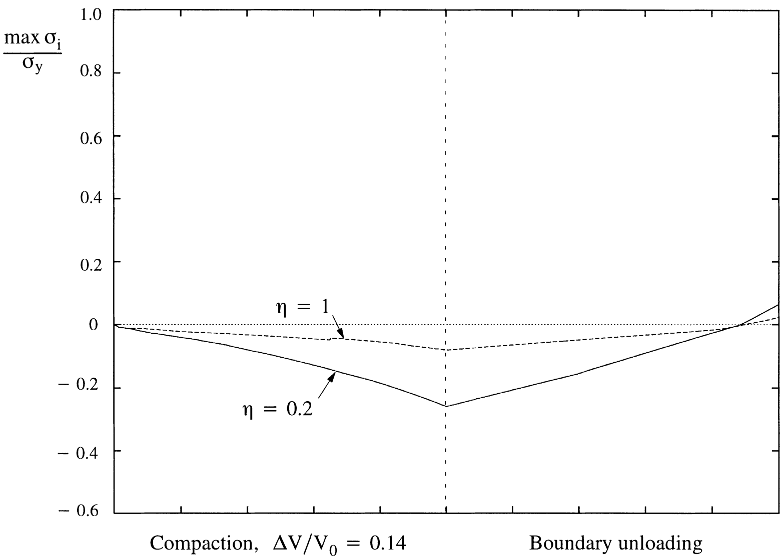

Fig. 9. The maximum principal stress , $\max(\sigma_i/\sigma_y)$, in the specimen during compaction, *Compaction III*, as well as *boundary unloading* for a material with fully sticking contacts between the particles, $\eta = 1$, and a material with a low inter-particle cohesive strength, $\eta = 0.2$.

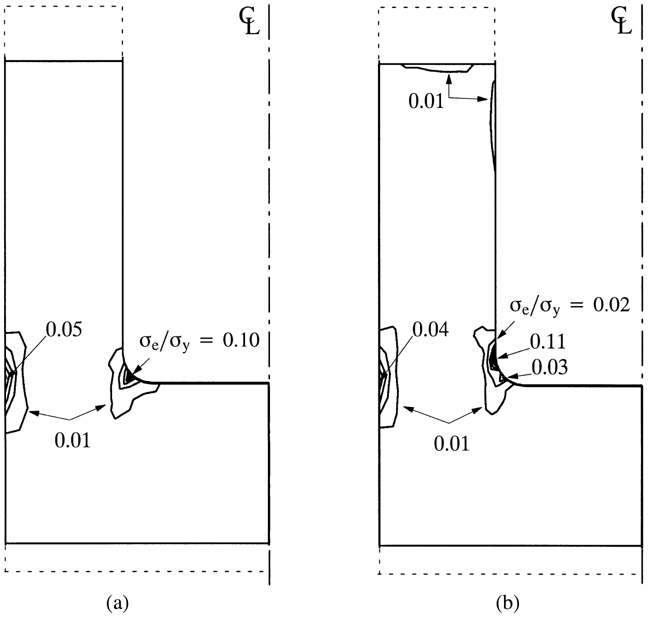

Fig. 10. Curves of constant von Mises stress, σ_e/σ_y, at $\Delta V/V_0 = 0.14$ after *compaction III* and subsequent *boundary unloading*: (a) fully sticking contacts between the powder particles, $\eta = 1$ and (b) low inter-particle cohesive strength, $\eta = 0.2$.

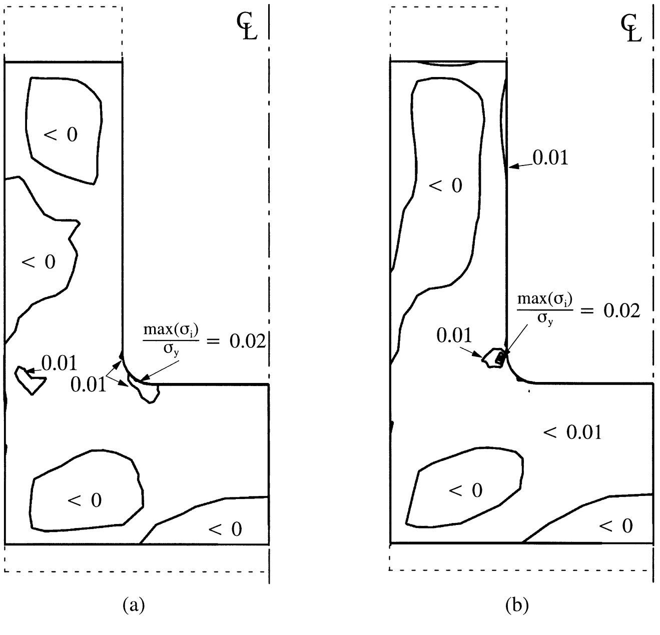

Fig. 11. Curves of constant maximum principal stress, $\max(\sigma_i)/\sigma_y$, at $\Delta V/V_0 = 0.14$ after *compaction III* and subsequent *boundary unloading*: (a) fully sticking contacts between the powder particels, $\eta = 1$ and (b) low inter-particle cohesive strength, $\eta = 0.2$.

6. Discussion

The porous materials used in cold powder compaction are not able to carry large tensile stresses because of the weak bonds between the powder particles. If a region in the porous aggregate is subjected to tensile stresses above a certain limit, brittle fracture is likely to occur depending on the maximum principal stress.

We conclude, that compaction with a velocity ratio between the punches P_1 and P_3 corresponding to the ratio of the height of the bottom of the cup, $H_o - H_i$ (see Fig. 1(b)), and the height of the cup wall, H_i, results in the most uniform and therefore optimal residual stress distribution. The way in which the cup is ejected is of less consequence for the final residual stress state. However, during the ejection process, maximum principal stresses occur which are higher than the final maximum stress in the unloaded specimen. In particular, the optimal compaction route among the three possibilities presented, *compaction III*, followed by *ejection I* results in a maximum principal stress during the ejection process which is twice as high as the final value (see Fig. 4). During most of the compaction and ejection processes, the maximum principal stress is located in the region at the inner, rounded corner of the cup, see label A in Fig. 4. But in some cases, the highest stress concentration occurs at the outer side of the cup where contact with the die wall is about to cease as the compact is ejected, see label B. In the actual process, this phenomenon often leads to fracture or damage of the specimen during the ejection process. The risk of fracture can be reduced by rounding-off the die wall edge at B as done in the present numerical study. Another possibility is to eject the specimen from the die while it is kept under axial pressure from the punches.

The simple *boundary unloading* scheme provides guidance on the residual stress distributions but it is not able to capture the observed maximum principal stress peaks during the ejection process; hence, using this method may be misleading if fracture is an issue.

Before unloading, the stress states in compacts of materials with different degrees of inter-particle cohesive strengths differ significantly, whereas the porosity distributions are almost identical. The average von Mises stress in a material with fully sticking contacts is 40–50% higher compared to that for the low cohesive strength material, whereas the hydrostatic pressure is much higher in the cup made of the low cohesive strength material. However, it has been shown that these differences in stress states almost disappear when the specimens are unloaded.

A material model in which a low or vanishing cohesive strength between the particles is present should be handled with care, since such a model causes numerical difficulties in pure tension; a failure criterion is necessary to model material separation. In order to avoid or at least minimize the level of tensile stresses in the specimen, the compaction route leading to the most uniform porosity and stress distribution from the combined material model results was chosen for the study of the effects of cohesive strength upon material compaction. It may be expected that for compacts with less uniform porosity distributions, the residual stress distributions are more sensitive to the degree of inter-particle cohesive strength.

Acknowledgements

The author wishes to thank Professor Viggo Tvergaard for the valuable help, comments and discussions.

References

Akisanya, A.R., Cocks, A.C.F., Fleck, N.A., 1997. The yield behaviour of metal powders. Int. J. Mech. Sci. 39 (12), 1315–1325.

Artz, E., 1982. The influence of an increasing particle co-ordination on the densification of spherical powders. Acta Metall. 30, 1883–1890.

Dowson, G., 1990. Powder Metallurgy: The Process and its Products. Adam Hilger, IOP Publishing, Boston, USA.

Drucker, D.C., Prager, W., 1952. Soil mechanics and plastic analysis or limit design. Q. Appl. Math. 10, 157–165.

Fischmeister, H.F., Artz, E., Olsson, L.R., 1978. Particle deformation and sliding during compaction of spherical powders: a study by quantitative metallography. Powder Metall. 21 (4), 179–187.

Fleck, N.A., 1995. On the cold compaction of powders. J. Mech. Phys. Solids 43, 1409–1431.

Fleck, N.A., Kuhn, L.T., McMeeking, R.M., 1992a. Yielding of metal powder bonded by isolated contacts. J. Mech. Phys. Solids 40 (5), 1139–1162.

Fleck, N.A., Otoyo, H., Needleman, A., 1992b. Indentation of porous solids. Int. J. Solids Struct. 29 (13), 1613–1636.

Gurson, A.L., 1977. Continuum theory of ductile rupture by void nucleation and growth: part I – yield criteria and flow rules for porous ductile media. J. Engng. Mater. Technol. ASME 99, 2–15.

Helle, A.A., Easterling, K.E., Ashby, M.F., 1985. Hot-isostatic pressing diagrams: new developments. Acta Metall. 33 (12), 2163–2174.

Hutchinson, J.W., 1973. Finite strain analysis of elastic–plastic solids and structures. In: Hartung, R.F. (Ed.), Numerical Solution of Nonlinear Structural Problems ASME 17, New York.

Kim, K.T., Lee, H.T., Kim, J.S., Kwon, Y.S., 1996. Analysis for die compaction of metal powders. Mechanics of Granular and Porous Materials. In: Fleck, N.A., Cocks, A.C.F. (Eds.), Proceedings of IUTAM Symposium. Cambridge, UK. Kluwer Academic Publishers, Netherlands (preprint).

Mesarovic, S.Dj., 1999. Finite element implementation of the micromechanics based constitutive model for stage I compaction of composite powders. Department of Engineering, University of Cambridge. Technical Report, ISSN 0309-7420. CUED/ C-MICROMECH/ TR, 22, 1–27.

Redanz, P., 1998. Numerical modelling of cold compaction of metal powder. Int. J. Mech. Sci. 40, 1175–1189.

Redanz, P., 1999. Numerical modelling of the powder compaction of a cup. Eur. J. Mech. A Solids 18, 399–413.

Redanz, P., Fleck, N.A., McMeeking, R.M., 1998. Failure of a porous solid from a deep notch. Int. J. Fracture 88, 187–203.

Redanz, P., Tvergaard, V., 1999. Analysis of shear band instabilities in sintered metals. Int. J. Solids Struct. 36, 3661–3676.

Schofield, A., Wroth, C.P., 1968. Critical State Soil Mechanics. McGraw-Hill, New York.

Shima, S., Oyane, M., 1976. Plasticity theory for porous metals. Int. J. Mech. Sci. 18, 285–291.

Tvergaard, V., 1981. Influence of voids on shear band instabilities under plane strain conditions. Int. J. Fracture 17, 389–407.

Tvergaard, V., 1982. On localisation in ductile materials containing spherical voids. Int. J. Fracture 18, 237–252.

Tvergaard, V., 1990. Effect of fibre debonding in a whisker-reinforced metal. Mater. Sci. Engng. A125, 203–213.